



The distinct PNA pattern induced by the South China Sea

Yinchen Zhang¹ · X. San Liang^{2,3,4}

Received: 10 May 2022 / Accepted: 23 November 2022

© The Author(s), under exclusive licence to Springer-Verlag GmbH Germany, part of Springer Nature 2022

Abstract

The Pacific–North American (PNA) teleconnection pattern has recently been found to be influenced by the South China Sea (SCS) sea surface temperature anomaly (SSTA). This study further demonstrates that, the SCS SSTA can induce a new type of PNA response. The SCS-induced PNA pattern and its evolution are shown to be distinctly different from its conventional counterparts and, particularly, the ENSO-induced pattern. In contrast to the observed conventional patterns, the SCS-induced PNA seems to agree remarkably well with the classical theory of Rossby wave propagation on a sphere by Hoskins and Karoly (1981), with the centers following the great circle route, and it shows a more zonally oriented new pathway of evolution led by a precursory center not seen before. Further study of the dynamical processes underlying the new PNA response reveals a specific air–sea interaction triggered by SCS SSTA, which results in an upper-level Rossby wave source and induces the precursory center. We remark that, although the SCS SSTA is relatively small in amplitude, it has an effect on PNA almost as conspicuous as that from ENSO.

Keywords South China Sea · Pacific–North American teleconnection pattern · Great circle · Tropical forcing · Air–sea interaction

1 Introduction

The Pacific–North American (PNA) teleconnection pattern is one of the most prominent low-frequency atmospheric modes, especially in boreal winter (Wallace and Gutzler 1981). The conventional PNA features a quasi-stationary wave train with four centers of action located over the subtropical Pacific, North Pacific, northwestern North America, and southeastern United States, respectively, and it is essentially barotropic in vertical. The PNA dominates the

hydroclimate variability of North America (e.g., Leathers et al. 1991; Liu et al. 2017) and exerts effects on far-reaching regions (e.g., L’Heureux et al. 2008; Drouard et al. 2015). A better understanding of PNA will improve climate prediction, especially for the intraseasonal prediction that is of growing importance (e.g., Baxter and Nigam 2013).

The generation of PNA has been extensively studied, with particular emphasis laid upon the role of tropical forcing. For example, it is believed that tropical forcing is important in realizing PNA as a dominant mode (e.g., Feldstein 2000; Mori and Watanabe 2008) and in determining its 2–3-week life cycle (e.g., Branstator 2014; Dai et al. 2017). Various known and unknown tropical forcings have been reported to account for the PNA formation, among which is our recent work (Zhang and Liang 2021) on the causal role of South China Sea (SCS) sea surface temperature anomaly (SSTA). This is the first time revealing that SCS may also impact PNA. Using a rigorously developed causal inference formalism, we showed that the causality is robust, and distinctly different from those bearing other origins. The positive (negative) propagating PNA-like response induced by positive (negative) SCS SSTA has also been revealed in numerical simulations.

✉ X. San Liang
xsliang@sml-zhuhai.cn

¹ School of Atmospheric Sciences, Nanjing University of Information Science and Technology, Nanjing 210044, China

² Division of Frontier Research, Southern Marine Science and Engineering Guangdong Laboratory (Zhuhai), Zhuhai 519000, China

³ Department of Atmospheric and Oceanic Sciences, Institute of Atmospheric Sciences, Fudan University, Shanghai 200438, China

⁴ IRDR ICoE on Risk Interconnectivity and Governance on Weather/Climate Extremes Impact and Public Health, Fudan University, Shanghai 200438, China

The newly revealed SCS impact on PNA is in addition to the impact of El Niño – Southern Oscillation (ENSO) that has long been studied: it is acknowledged that more positive (negative)-phase PNA events occur during El Niño (La Niña) periods, and PNA was once considered as the extratropical response to ENSO (e.g., Horel and Wallace 1981; Shukla and Wallace 1983). However, ENSO cannot fully explain the PNA (e.g., Renshaw et al. 1998; Straus and Shukla 2002); reportedly it accounts for only about 29% of the PNA variance (Li et al. 2019). This is consistent with the newly revealed causal role of SCS.

It is observed that PNA is not a single pattern, but a continuum mixed with different patterns of similar structures originating from internal dynamics or induced by various external forcings (e.g., Johnson and Feldstein 2010; Yuan et al. 2015; Dai et al. 2017). As well known, the PNA response to the traditional Eastern Pacific (EP) El Niño and that to the Central Pacific (CP) El Niño or El Niño Modoki (e.g., Yu and Kao 2007; Ashok et al. 2007) are not identical (e.g., Weng et al. 2009; Yu et al. 2012). It has been argued that different responses may be attributed to the different locations (especially longitudinal locations) of the forcings (e.g., Alexander et al. 2002; Barsugli and Sardeshmukh 2002). As SCS serves as another source of tropical forcing that is located far away westward, we hence conjecture that the PNA response induced by SCS may also be a new pattern. To identify the SCS-induced PNA pattern thus makes the goal of this study.

In the following, we first introduce the data and methods. Sections 3 and 4 are the results, and Sect. 5 summarizes the whole study.

2 Data and PNA identification

The dataset used for this study is the fifth generation European Centre for Medium-Range Weather Forecasts (ECMWF) reanalysis for the global climate (ERA5; Hersbach et al. 2020). The daily data from November 1979 to March 2019 with a horizontal resolution of $0.5^\circ \times 0.5^\circ$ is taken. The variables include geopotential height (Z), zonal (u) and meridional (v) winds, vertical velocity (ω), and temperature (T) for 28 pressure levels, along with latent and sensible upward surface heat fluxes, and sea surface temperature (SST). The daily anomaly (denoted by prime) is obtained by subtracting the 1981–2010 daily calendar climatology to remove the seasonal cycle, followed by an application of a 10-day low-pass filter (e.g., Mori and Watanabe 2008).

The PNA is identified with the widely-used rotated empirical orthogonal function (REOF) analysis, which is applied to the 500-hPa geopotential height anomaly (Z') over the North Pacific sector (0° – 90° N, 120° E– 60° W) for the extended boreal winters (November–March) from 1979/80

to 2018/19. The PNA mode is taken as the first REOF mode by rotating 5 leading modes by the so-called *varimax* criterion (e.g., Barnston and Livezey 1987; Lian and Chen 2012). The time series corresponding to such an REOF mode is then normalized. This is the PNA index. A positive (negative) PNA event is identified when the index is above 1.2 (below -1.2) and lasts for at least 5 days. Those events far from monotonic growth and decay are discarded. The identified events will be used for composite analyses. For each event, we define the peak day as day 0. Generally, day -9 is regarded as the onset of a PNA life cycle.

The PNA state can be characterized by the anomalous quasi-geostrophic stream function (ψ') and the wave activity flux (WAF). The former is defined as $\psi = \Phi/f$, where Φ is the geopotential and f the Coriolis parameter; the latter has a horizontal component which can be simply expressed as

$$\text{WAF} = \frac{1}{2|\mathbf{U}|} \left(\begin{array}{l} U(\psi_x'^2 - \psi' \psi_{xx}') + V(\psi_x' \psi_y' - \psi' \psi_{xy}') \\ U(\psi_x' \psi_y' - \psi' \psi_{xy}') + V(\psi_y'^2 - \psi' \psi_{yy}') \end{array} \right), \quad (1)$$

where subscripts denote partial derivatives, and $\mathbf{U} = (U, V)$ the climatological wind. For details, see Takaya and Nakamura (2001). A chain of ψ' with alternate signs represents the wave train, and the associated WAF indicates the direction of the wave energy propagation. Considering the quasi-geostrophic approximation, such fields are calculated poleward of 5° N.

3 Features of the SCS-induced PNA

According to the above-mentioned criteria, 35 positive and 31 negative PNA events are identified, from which we are about to identify the SCS-induced PNA. As reported in Zhang and Liang (2021) through causal inference with the rigorously formulated information flow, together with numerical modeling, PNA can be causally influenced by SCS SSTA, in addition to ENSO. These two must be distinguished, and this can be done by taking into account the specific conditions of the preceding SSTA in the tropics.

A PNA event is considered as SCS-induced when occurring during non-ENSO periods and preceded by the active SCS SSTA, which is relatively strong (referring to the standard deviation) and positively correlated with the PNA phase (as previously revealed). Here the SCS SSTA is a regional averaged series over (3.5° – 21.5° N, 104.5° – 118.5° E). We also need the aid of the ENSO-related SSTA, which is defined as the average over the Niño 3.4 region. Accordingly, 6 positive and 5 negative SCS-induced PNA events are identified (their peak days are listed in Table 1). Likewise, the selected ENSO-induced events occur during ENSO episodes

Table 1 Peak days for the phases of the SCS- and ENSO-induced PNA events

	SCS-induced	ENSO-induced
Positive-phase	10/26/1980, 11/11/1981, 12/27/2000, 11/12/2001, 11/06/2016, 02/13/2017	02/26/1980, 01/27/1983, 03/11/1983, 02/03/1987, 02/26/1992, 02/05/1995, 02/02/1998, 12/25/2009
Negative-phase	03/06/1982, 12/23/1990, 12/17/1992, 01/16/2002, 01/31/2015	03/05/1985, 02/10/2001, 01/21/2006, 02/02/2008, 02/25/2011, 02/28/2012

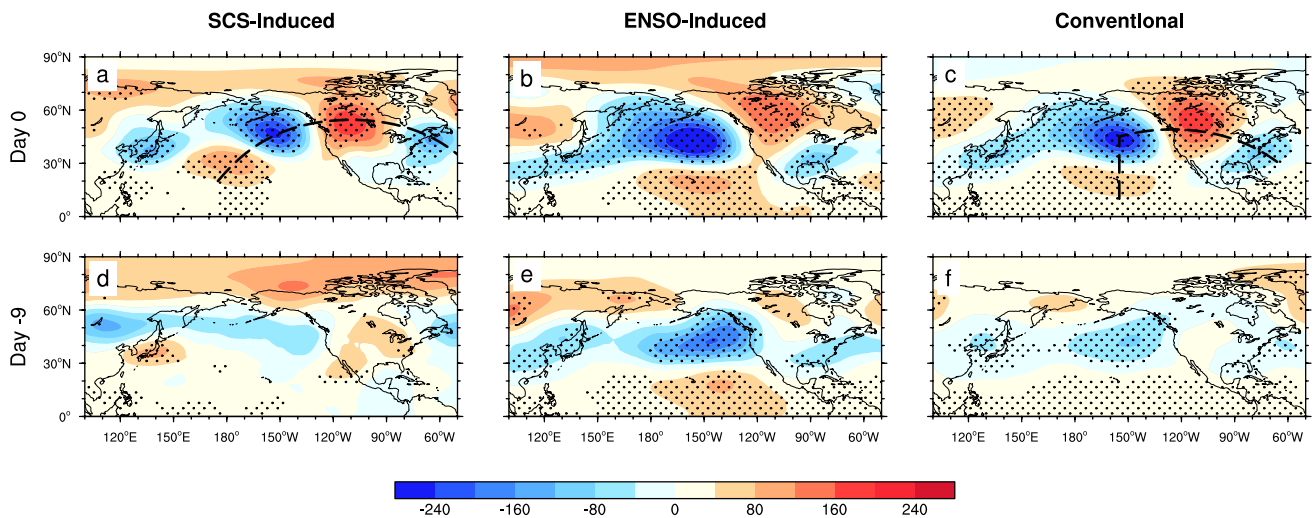


Fig. 1 Composite maps of the 250-hPa geopotential height anomaly (Z') (unit: m) for the positive phase of the (left) SCS-induced, (middle) ENSO-induced and (right) conventional PNAs on (upper) day 0 and (lower) day -9. The stippled regions are significant at the 90%

confidence level based on the Student's t-test. The dashed curve in **a** indicates the geodesic (great circle) from (20°N, 175°E) to (35°N, 50°W), and that in **c** indicates the route from (10°N, 155°W) to (45°N, 155°W) and then to (30°N, 65°W) along the great circle

and when the SCS SSTA is relatively weak, and there are 8 positive and 6 negative events identified (Table 1). For the purpose of this study, the CP and EP El Niños are not distinguished. Hereafter, the fields composited for the total PNA events will represent the conventional PNA features, and those for the selected SCS-induced and ENSO-induced PNA events are considered to solely reflect the SCS and ENSO effects, respectively (but note that their effects are not limited to these selected events).

Then we will investigate and distinguish the features of the SCS-induced PNA via composite analyses on each phase of the above three types of PNA events. The PNA pattern can be seen in the commonly used Z' fields at different levels due to its equivalent barotropic structure, and it is clearer with larger amplitude in the upper troposphere, say, 250 hPa. The composites of the 250-hPa Z' for the three types of positive-phase PNA events at day 0 are shown in Fig. 1. For all types, the well-known quadrupolar structure of PNA is clearly captured; especially, the ENSO-induced and conventional PNA patterns are well reproduced (Fig. 1b and c) according to previous studies (e.g., Chen et al. 2018; Li et al. 2019). By comparison, the SCS-induced PNA pattern (Fig. 1a) is somewhat distinctly different from these

two patterns: Its anomaly centers are shifted, revealing a more scattered distribution; this is especially the case for the subtropical Pacific center and the southeastern United States center, which are respectively more westward and northeastward.

A conspicuous feature of the SCS-induced PNA is that the centers follow well the great circle route (marked with dashed curve in Fig. 1a), seemingly agreeing well with the theory of Rossby wave propagation on a sphere for interpreting PNA formation (Hoskins and Karoly 1981). In contrast, the conventional pattern, and the ENSO-induced pattern in particular, are rather convergent, bearing a saddle-like shape. Such route difference implies a new pathway of evolution, which will be discussed below.

The uniqueness of the SCS-induced PNA has already appeared at the event onset around day -9 (Fig. 1d). Especially, there exists a distinct center of positive anomaly (namely anticyclonic center) over the Yellow Sea and Japan (to the northeast of SCS), which is relevant to the subtropical Pacific center of PNA at day 0. This precursory center detected for the SCS-induced PNA is totally absent in the fields associated with the ENSO-induced (Fig. 1e) and conventional PNAs (Fig. 1f). As for the onset of the

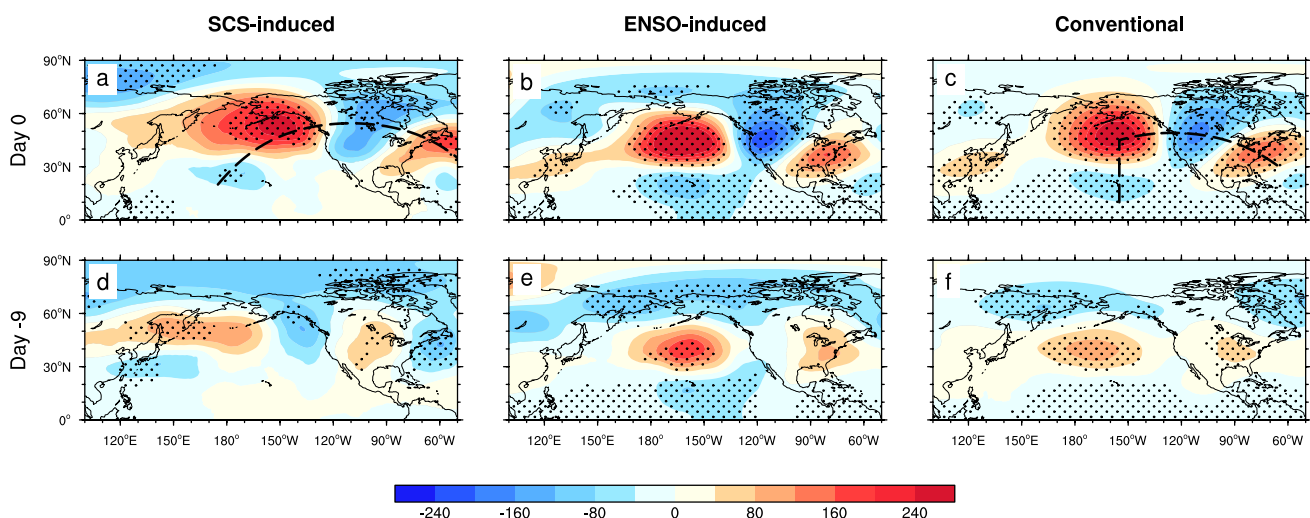


Fig. 2 As in Fig. 1, but for the negative phase

ENSO-induced PNA, it is featured by the embryo of two upstream centers over the Pacific (Fig. 1e), which manifests as a meridional dipole. Clearly, the difference between the two types of PNA is more significant at the onset than at maturity (day 0), implying the different driving forcings, e.g., those associated with SCS and ENSO, respectively.

Note that all the features demonstrated above are tested to be significant. This is clear in Fig. 1, in which the stippling denotes regions significant at the 90% confidence level based on the Student's *t*-test.

For the negative-phase counterparts (Fig. 2), similar features are observed, including the shifted and great-circle arranged centers of the SCS-induced PNA (Fig. 2a) and the precursory center to the northeast of SCS (Fig. 2d). The difference is that the high-latitude centers, especially the North Pacific center, are stronger, and more obviously, larger in area. Such an asymmetry also exists for the ENSO-induced and conventional PNAs, although not so obvious. Besides, for the SCS-induced negative PNA, the subtropical Pacific center is somewhat weaker (Fig. 2a), and at day -9, the relevant precursory center appears to have moved downstream already (Fig. 2d). This may imply the earlier onset of PNA and earlier propagation of wave energy downstream to the North Pacific. These phenomena are reminiscent of previous findings that the negative PNA tends to have larger amplitude and longer lifetime (e.g., Palmer 1988; Corti and Palmer 1997; Luo et al. 2020). The asymmetry for the SCS-induced PNA seems to be stronger in comparison to its conventional counterparts.

The horizontal wind fields, which reportedly have a high *teleconnectivity* (e.g., Athanasiadis et al. 2010), reveal consistent features as above (not shown). The aforementioned great circle route that the SCS-induced PNA centers follow still exists in the corresponding 250-hPa composite

anomalous horizontal wind field. Compared to their ENSO-induced and conventional counterparts, the two convergence belts of strong anomalous wind respectively between the two upstream and two downstream centers for the SCS-induced PNA are located more westward and northeastward, leading to a shift of the impact. The precursory center and phase asymmetry for the SCS-induced PNA are also seen here.

The vertical structure of the SCS-induced PNA is manifested by the cross-sectional distribution of the composited geopotential height anomaly (Fig. 3a and c; for both phases) along the great circle as marked in Fig. 1a. For comparison, a cross section is also chosen for the conventional PNA (Fig. 3b and d), as marked in Fig. 1c. The two sections are respectively designed to cross all the four PNA centers in order to capture the vertical structures in full. For all cases, the equivalent barotropic nature of PNA is well displayed (Fig. 3).

For each vertical structure, the centers are regularly arranged in height by and large, except that the subtropical Pacific center is relatively confined at upper levels with weaker amplitude. It is reminiscent of the different formations of upstream and downstream centers (Feldstein 2002), and the subtropical Pacific center could be the best reflection of different effects from upstream processes. Indeed, such a center is where the two types of sections mainly differ; for the SCS-induced PNA, the center is located relatively lower than the conventional counterpart. Besides, the phase asymmetry (Fig. 3a and b vs. c and d) is still visible in vertical and appears stronger for the SCS-induced PNA.

Despite the minor differences above, the two types of PNA are rather similar in vertical. As can be seen, the uniqueness of the SCS-induced PNA is essentially in its horizontal distribution.

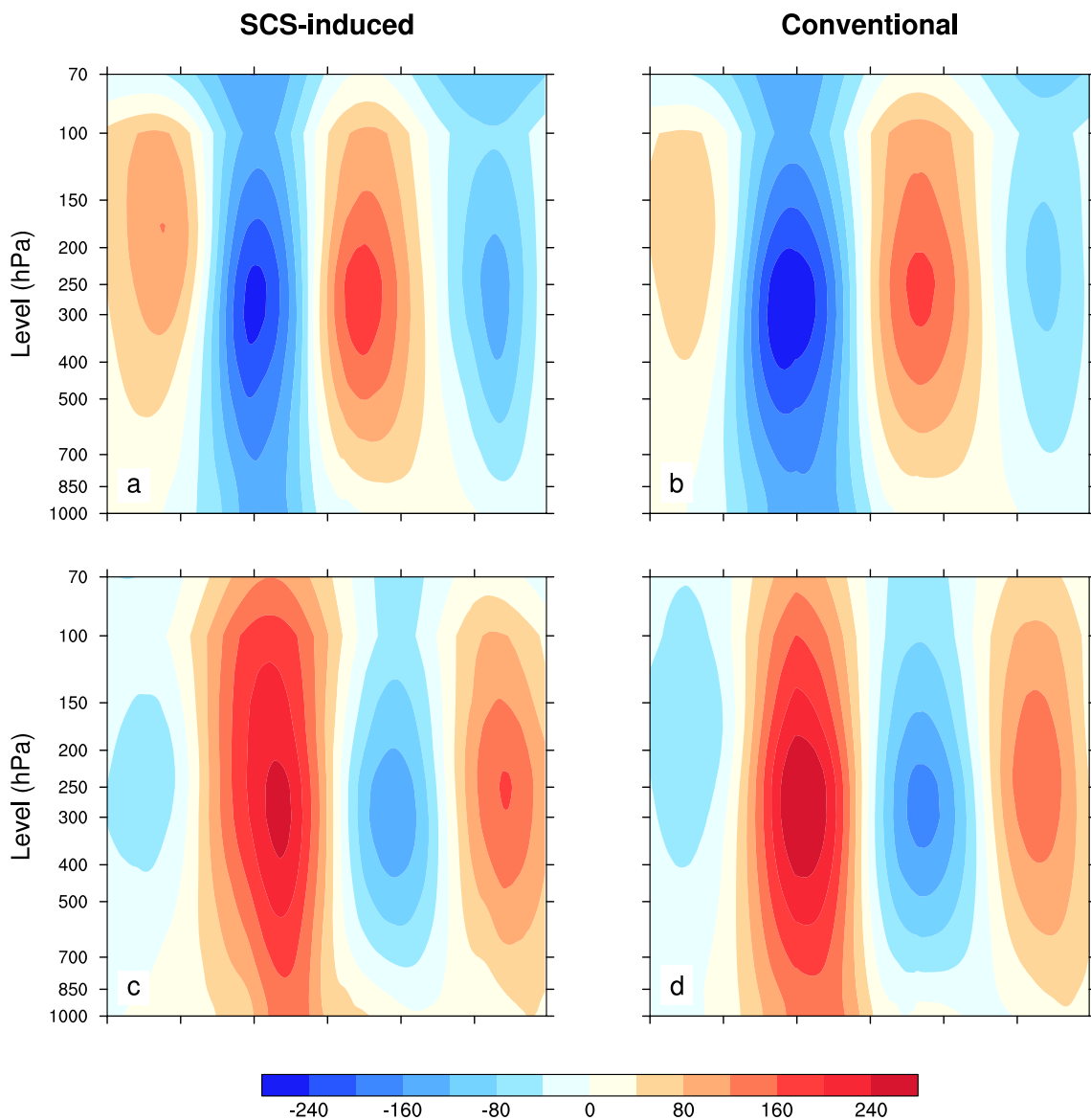


Fig. 3 Vertical distributions of composited geopotential height anomaly (Z') (unit: m) for the (upper) positive and (lower) negative phases of the (left) SCS-induced and (right) conventional PNAs on day 0. The horizontal axes are respectively along the routes as marked in Fig. 1a and c

Further, the evolutions of different types of PNA are examined, via the composited 250-hPa ψ' and WAF snapshots. For the positive-phase SCS-induced PNA (left column of Fig. 4), by day -10 , the aforesaid precursory anticyclonic center has formed to the northeast of SCS (marked with black box), near the latitude where the Asian westerly jet lies. Afterwards, the precursory center propagates downstream along the jet axis due to the waveguide (e.g., Branstator 1983; Hoskins and Ambrizzi 1993). Around day -4 , such a center reaches the jet exit region, which is known as a key region with barotropic amplification (e.g., Simmons et al. 1983; Feldstein 2002). As can be seen, it grows to a larger amplitude, along with stronger wave activity. Meanwhile, the

wave propagation escapes from the waveguide trap, dispersing along the great circle from the jet exit to North America. There is also a weaker southern branch of dispersion, along which the precursory center gradually merges into the PNA embryo. While upstream of the jet, there follows an opposite-sign (cyclonic) center. As the wave energy propagates to North America, the PNA pattern matures at day 0.

The evolution features above do not show up in the ENSO-induced PNA (middle column of Fig. 4); especially, the highlighted precursory center and a clear eastward wave pathway are missing. Instead, the wave train induced by ENSO shows a more poleward pathway; it initially appears as a meridional dipole in the eastern Pacific. The barotropic

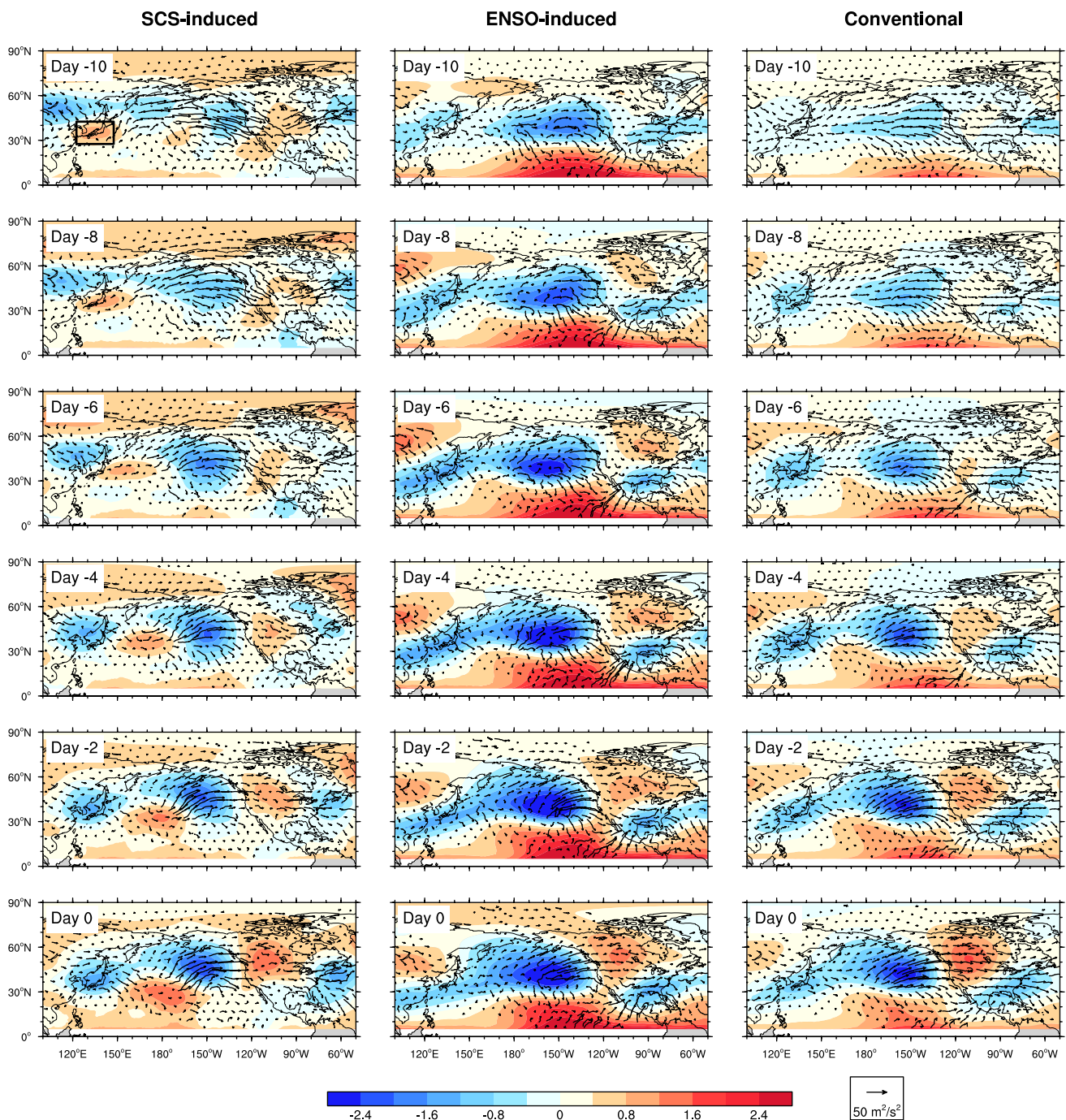


Fig. 4 Composites evolutions for the positive-phase patterns of the (left) SCS-induced, (middle) ENSO-induced and (right) conventional PNAs from day –10 to day 0 with an interval of 2 days. The fields are

the 250-hPa ψ' (shading; unit: $10^7 \text{ m}^2 \text{ s}^{-1}$) and WAF (arrows; scaling: $50 \text{ m}^2 \text{ s}^{-2}$). Black box in the first subplot indicates the location of the precursor center

amplification at the jet exit takes place later as well; it is characterized by an amplified WAF. Then the wave activity disperses to North America, where the PNA pattern gradually matures. A similar evolution is also seen in the conventional PNA (right column of Fig. 4).

As is shown, the combined action of the distinct SCS induction and jet effect determines the aforementioned great circle route. The SCS-induced response is originally generated on the jet axis and trapped until escaping the jet exit. Away from strong gradients, the basic flow becomes relatively uniform with constant angular velocity, under which

condition the dispersion theoretically follows a great circle (e.g., Hoskins and Karoly 1981; Yang and Hoskins 1996; Wirth et al. 2018). That is to say, this type of dispersion accounts for the formation of all the four centers of the SCS-induced PNA, leading to a great circle route, in contrast to the ENSO-induced PNA where only the downstream centers are as this (consistent with Feldstein 2002).

Besides, in all types of evolution, the upstream cyclonic center is a general feature, as observed in the previous studies (e.g., Mori and Watanabe 2008; Baxter and Nigam 2013); it may be associated with the Eurasian wave train that benefits the amplification (e.g., Dai et al. 2017). In contrast, the precursory anticyclonic center is only seen in the SCS-induced PNA evolution.

The negative-phase evolutions (Fig. 5) generally resemble their positive-phase counterparts above, except for an opposite sign, and some phase asymmetries in amplitude and lifetime. Especially, the SCS-related precursory center for the negative phase seems to have formed earlier and moved more downstream at day -10 . Accordingly, the wave activity appears to propagate earlier to North Pacific, which may well account for the stronger North Pacific center at day 0 (also shown in Fig. 2).

According to the evolutions illustrated above, it is worth noting that for different types of PNAs, initially quite different perturbations eventually organize into similar patterns (although not identical). It is consistent with the suggestion that perturbations aroused by different mechanisms can evolve into some certain circulations (e.g., PNA), as long as the spatial structure matches the unstable normal mode (e.g., Simmons et al. 1983).

4 Processes underlying the SCS excitation

The SCS, as a large semi-closed marginal sea with considerable upper-layer heat content, displays remarkable air-sea interaction which allows extensive effects on the atmosphere (e.g., Liu et al. 2004; Wang et al. 2007; Roxy and Tanimoto 2012; He and Wu 2013; Gong et al. 2019) and can also be key to triggering the PNA. In this sense, the air-sea interaction in the SCS excitation of PNA should be analogous to that in the ENSO excitation, which has been well established: the ENSO-related SSTA modulates atmospheric heating and convection through surface heat flux, then the resultant anomalous divergence generates the Rossby wave source where the wave train response is excited, affecting the PNA formation (e.g., Shukla and Wallace 1983; Trenberth et al. 1998). We henceforth follow this clue to diagnose the SCS excitation.

Figure 6 shows the preceding SSTA distributions for different types of PNA near the event onset, say, at day -9 . For both phases of the SCS-induced type (Figs. 6a and d), large

areas of high SSTA values are clearly seen within the SCS (as marked with black boxes). Especially, the SSTA appears stronger in the northern SCS, consistent with the suggestion that the oceanic forcing is dominant in the northern SCS during winter (He and Wu 2013). Meanwhile in the central and eastern equatorial Pacific, no significant ENSO-related SSTA appears, and the existing SSTA is even opposite in sign to the SCS SSTA and the PNA phase. Likewise, for the ENSO-induced type, the distributions of preceding SSTA in the equatorial Pacific are quite reminiscent of the typical ENSO patterns, while the SCS SSTA is not active (Fig. 6b and e). Incidentally, the ENSO asymmetry is also captured, i.e., the La Niña-related pattern is usually weaker in amplitude and westward-shifted. For the SSTA distribution preceding the conventional PNA (Fig. 6c and f), the signals driven by different contributing forcings are mixed up, leading to the alleviated SSTA distribution. The above results confirm that the SCS-induced PNA is indeed preceded by a unique oceanic thermal condition dominated by the SCS SSTA.

The above snapshots on day -9 give the spatial structure of the aforementioned preceding SSTA. To further explore the thermal conditions which actually continuously vary with time, we show in Fig. 7 the preceding SCS and Niño 3.4 SSTA series, which are formed by taking regional averages, for different PNA types. The displayed general thermal conditions are consistent with those shown in the spatial snapshots; in particular, only the SCS-induced PNA is preceded by an active SCS SSTA (see the upper row), and only active SCS SSTA precedes this type (see the left column).

A notable feature is that the SCS SSTA variations preceding the two phases of the SCS-induced PNA are asymmetric in time (slightly in amplitude) (Fig. 7a). In other words, the evolution lifetimes of PNAs in response to positive and negative SCS SSTA are asymmetric, i.e., positive (negative) PNA matures approximately 10 (20) days after the peak day of positive (negative) SCS SSTA that follows an obviously rise (fall) about 5 days earlier. By comparison, the Niño 3.4 SSTA (lower row) is only asymmetric in amplitude, and there is barely any variation. Besides, the order of magnitude of the SCS SSTA is smaller, while the preceding SCS SSTA for the SCS-induced PNA (Fig. 7a) is relatively strong (greater than one standard deviation).

The SSTA condition preceding the SCS-induced PNA as illustrated above is supposed to exert forcing on the atmosphere mainly through surface heat flux (SHF). The SHF contains the latent type related to evaporation and condensation and the sensible type related to the temperature difference, where the former predominates in the oceanic forcing.

Accordingly, the distribution of the sum of latent and sensible upward SHF anomalies (the former occupies the main proportion; not shown) preceding the SCS-induced PNA is examined. Considering the lifetime asymmetry mentioned

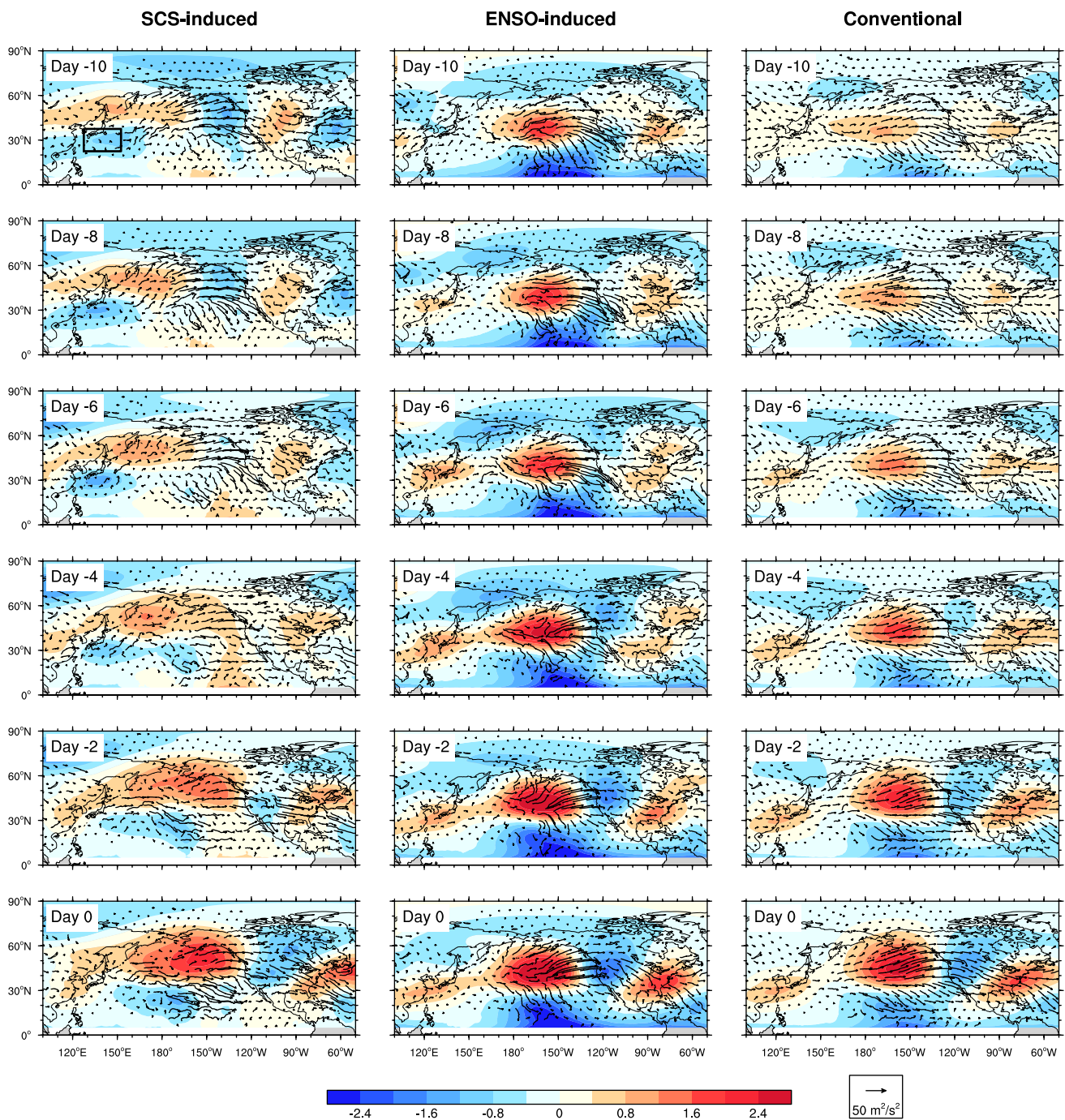


Fig. 5 As in Fig. 4, but for the negative phase

above, the fields from day -15 (-25) to day -11 (-21) for the positive (negative) phase are shown (Fig. 8). During the periods, considerable upward SHF anomalies are obviously seen within the SCS, indicating the strong air-sea interaction driven by the SCS SSTA. As time goes on, the anomalies steadily amplify and extend northeastward, well synchronized with the SCS SSTA growth (Fig. 7a). The action of SHF anomalies lasts for days, exerting continuous effects on

the atmosphere. Note that the negative SCS SHF anomalies (right column) indicate the weakening of the upward SCS forcing but not the direction reversal of the forcing, in that the tropical ocean always acts as a heat source in winter (not shown).

Through the anomalous SHF especially the latent component, the SCS will cause anomalous heating and cooling to the overlying atmosphere. Generally, positive SSTA (vice

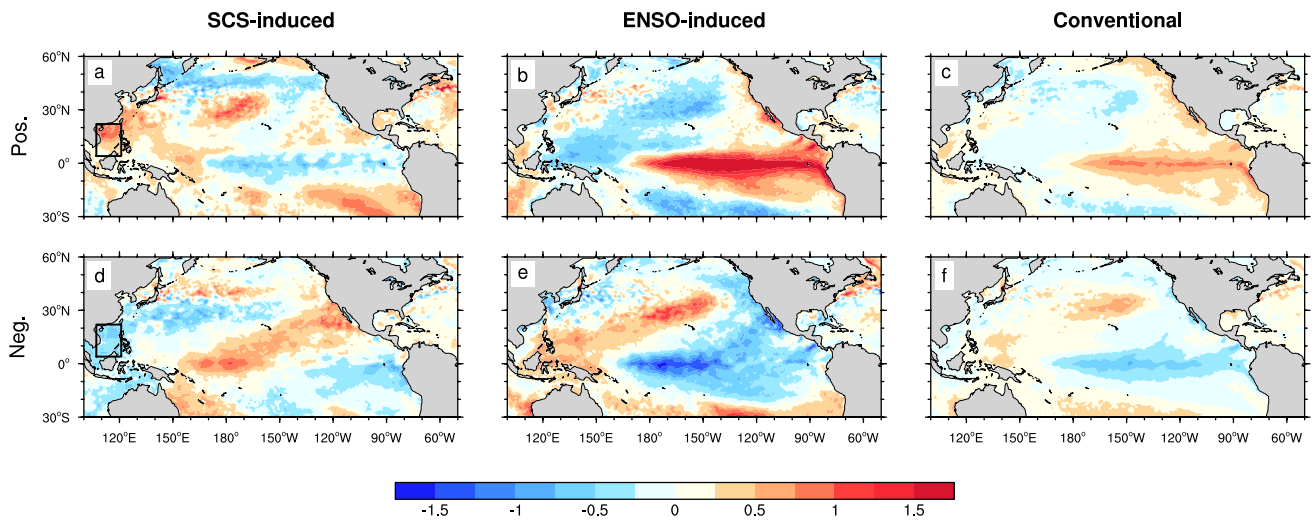


Fig. 6 Composite maps of the preceding SSTA (unit: °C) for the (upper) positive and (lower) negative phases of the (left) SCS-induced, (middle) ENSO-induced and (right) conventional PNAs on day -9 . Black boxes in **a** and **d** highlight the SCS region

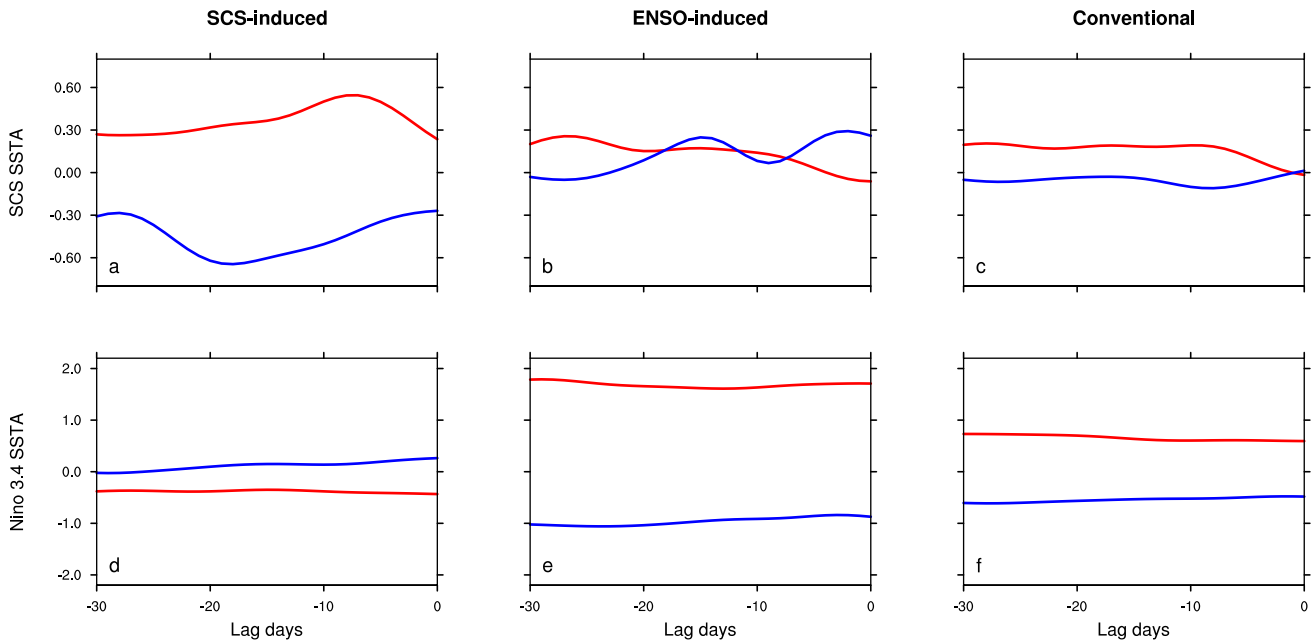


Fig. 7 Compositing time series of the preceding (upper) SCS and (lower) Niño 3.4 regionally averaged SSTA (unit: °C) for the (red lines) positive and (blue lines) negative phases of the (left) SCS-induced, (middle) ENSO-induced and (right) conventional PNAs from day -30 to day 0

versa for the negative SSTA) enhances surface evaporation. When the moisture condenses, heat is released (reflected by the latent SHF), causing the atmospheric diabatic heating and the resultant convection and ascending motion; low-level convergence and upper-level divergence are then aroused (see a review in Cronin et al. 2019).

As expected, this classical scenario of air-sea interaction is observed within the SCS. On day -15 for the positive SCS-induced PNA (early stage of SCS warming), strong

ascending motion (negative anomalous vertical velocity ω') takes place over the SCS (Fig. 9a), appearing deeply throughout the troposphere with a slight northward tilt. Accordingly, the anomalous convergence at the surface and divergence aloft are caused (contours in Fig. 9a). Taking 950 hPa and 250 hPa as representative levels, the convergence and divergence patterns spreading over the SCS and southern China are shown in Fig. 9b and c. The fields induced by the SCS cooling (lower row of Fig. 9) generally

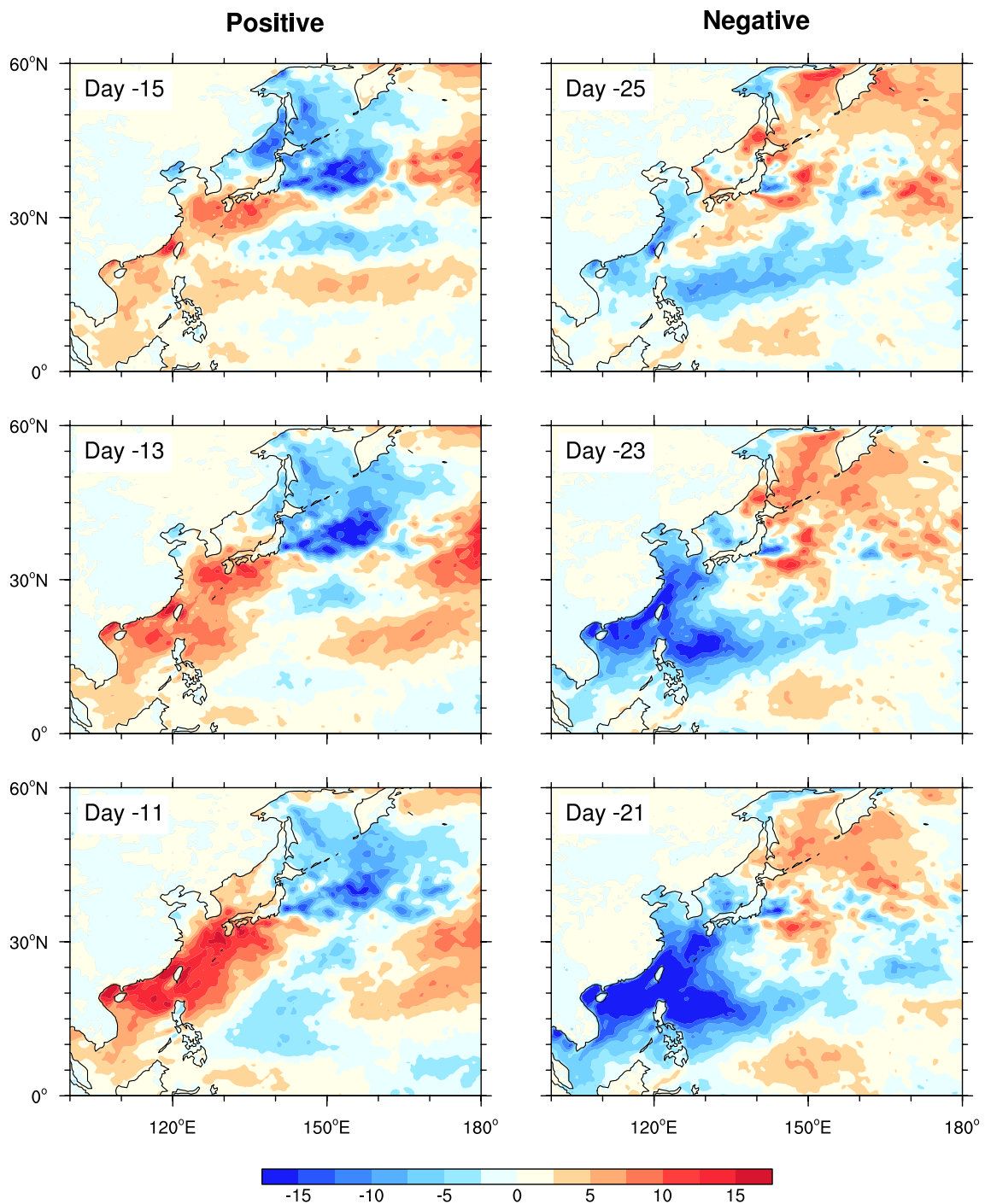


Fig. 8 Composite maps of the sum of latent and sensible upward surface heat flux anomalies (unit: W m^{-2}) preceding the (left) positive and (right) negative phases of the SCS-induced PNAs respectively

from day -15 to day -11, and from day -25 to day -21, with an interval of 2 days

belong to the opposite situation, except for a stronger intensity, which is consistent with the aforementioned phase asymmetry. In experiencing this, the influence of the SCS SSTA eventually reaches the upper-level atmosphere.

As the anomalous upper-level divergence/convergence is aroused, its interaction with the existing vorticity will contribute to generating Rossby wave sources, making the source for a wave train in response. This can be diagnosed

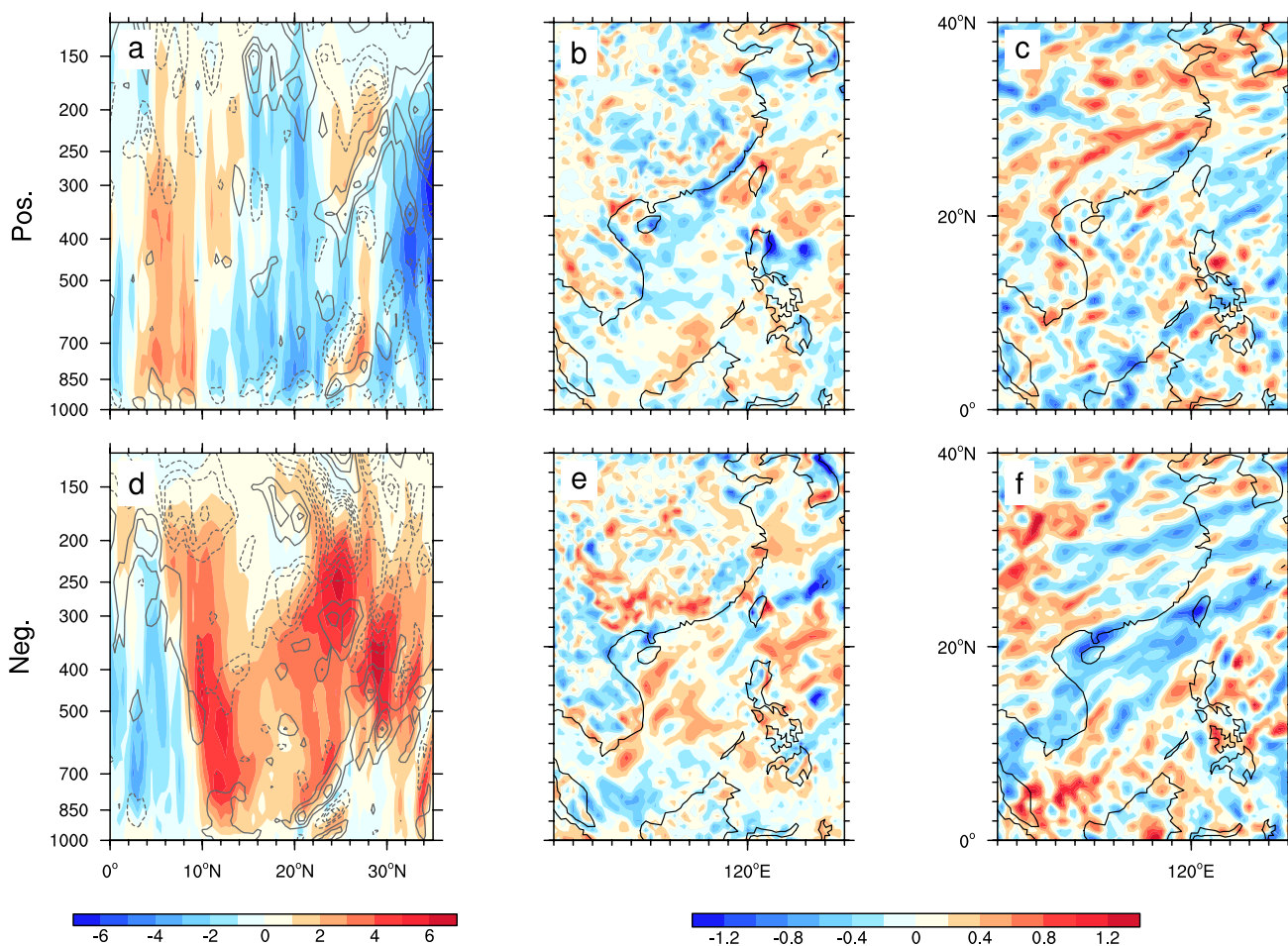


Fig. 9 Composites of the (left) latitude–height diagrams of the anomalous vertical velocity (shading; unit: 10^{-2} Pa s^{-1}) and divergence (contours; interval: 1.5×10^{-6} s^{-1}) averaged from 110° to 120°E, and (middle) the 950-hPa and (right) 250-hPa anomalous divergence

(unit: 10^{-5} s^{-1}) preceding the (upper) positive and (lower) negative phases of the SCS-induced PNAs respectively on day –15 and day –25

following Sardeshmukh and Hoskins (1988), as demonstrated below.

Considering the barotropic vorticity equation without friction:

$$\left(\frac{\partial}{\partial t} + \mathbf{v}_\psi \cdot \nabla\right)\zeta_a = -\zeta_a D - \mathbf{v}_\chi \cdot \nabla\zeta_a, \quad (2)$$

where \mathbf{v}_ψ and \mathbf{v}_χ are rotational and divergent components of the horizontal wind, ζ_a the absolute vorticity composed of relative vorticity (ζ) and Coriolis parameter (f), and D the divergence. The right-hand side is namely the Rossby wave source term, in balance with the left-hand side related to the propagation. After linearization and filtering, the anomalous low-frequency wave source (S_L) is derived (Mori and Watanabe 2008):

$$S_L = -\left(\bar{\zeta} + f\right)D_L - \mathbf{v}_{\chi L} \cdot \nabla\left(\bar{\zeta} + f\right) - \zeta_L \bar{D} - \bar{\mathbf{v}}_\chi \cdot \nabla\zeta_L, \quad (3)$$

where the overbar denotes the climatology, and the subscript L denotes the filtered low-frequency anomaly same as that in Sect. 2. It can be divided into divergence (terms 1 and 3) and advection (terms 2 and 4) components, where terms 3 and 4 are smaller in magnitude and can be omitted.

The anomalous upper-level wave source (250-hPa S_L) and associated terms preceding the SCS-induced PNA are diagnosed. Their snapshots on day –10 (–20) for positive (negative) phase are taken as representatives (Figs. 10 and 11). As is shown, the anomalous upper-level divergence (D_L) (shaded in Fig. 10a) has been aroused by the positive SCS SSTA and spread over the SCS and southern China. Noticeably, the northern portion of the wide-spread divergence pattern coincides with the Asian westerly jet that provides strong climatological absolute vorticity ($\bar{\zeta} + f$) (see the dense contours in Fig. 10a). Hence, the SCS-induced divergence interacts with the existing vorticity, causing the vortex stretching. The divergence term $-\left(\bar{\zeta} + f\right)D_L$ is thus gener-

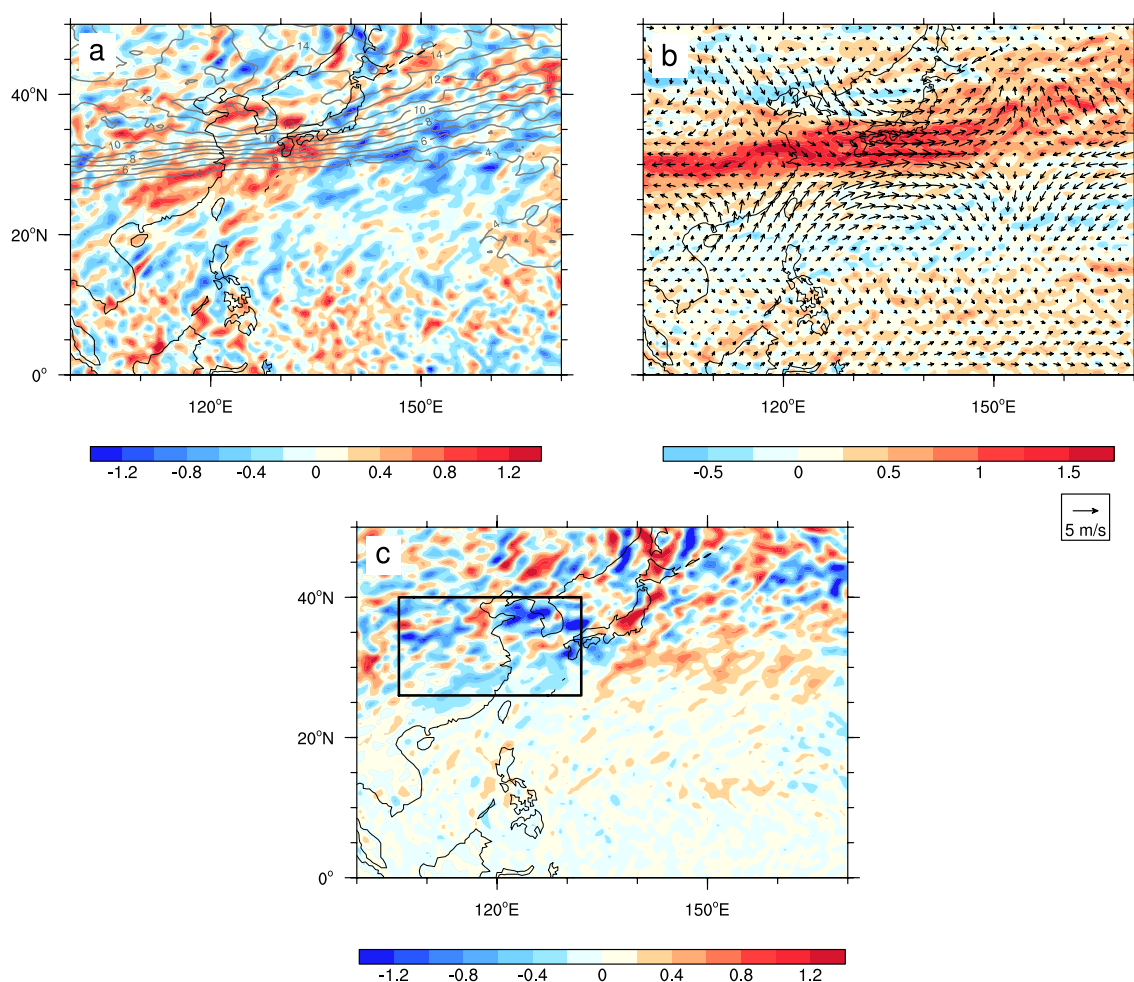


Fig. 10 Composite maps of the 250-hPa S_L with associated terms preceding the positive phase of the SCS-induced PNA on day -10. **a** D_L (shading; unit: 10^{-5} s^{-1}) and $\bar{\zeta} + f$ (poleward-ascending con-

tours; unit: 10^{-5} s^{-1}). **b** Meridional gradient of $\bar{\zeta} + f$ (shading; unit: $10^{-10} \text{ m}^{-1} \text{ s}^{-1}$) and $\mathbf{v}_{\chi L}$ (arrows; in 5 m s^{-1}). **c** S_L (shading; unit: 10^{-9} s^{-2}). Black box in **c** marks the SCS-induced S_L region

ated by their combined action. On the other hand, the jet axis also exhibits the positive maximum of the meridional gradient of vorticity (the major portion of $\nabla(\bar{\zeta} + f)$) (shaded in Fig. 10b). As the anomalous diverging divergent wind ($\mathbf{v}_{\chi L}$) (arrows in Fig. 10b) crosses the jet axis, the advection term $-\mathbf{v}_{\chi L} \cdot \nabla(\bar{\zeta} + f)$ is thus favored by their interaction. Due to the above two predominant effects, the negative total wave source (S_L) is generated, whose pattern is prominent to the north of SCS (as marked in Fig. 10c), just near the jet core. As a source of negative vorticity, such a wave source region thus gives rise to an initial anticyclonic anomalous center slightly downstream (see Fig. 4), which has been identified to be the precursor of the positive PNA response to the SCS SSTA. As well as the aforesaid continuous air-sea interaction, the action of wave source lasts for days, supplying vorticity for the precursory center excitation.

Likewise, for the suppressed forcing by negative SCS SSTA, strong anomalous upper-level convergence (Fig. 11a) and converging divergent wind across the jet (Fig. 11b) are triggered, which then generate the positive S_L pattern to the north of SCS (as marked in Fig. 11c) via the interactions with the jet vorticity effects. With the continuous supply of positive vorticity, the precursory cyclonic center (see Fig. 5) leading the negative PNA response to the SCS SSTA is excited.

To sum up, active SCS SSTA modulates the atmospheric diabatic heating through the surface heat flux, and then arouses anomalous upper-level divergence/convergence, which, jointly with the jet vorticity effects, generates a Rossby wave source, from which a new PNA led by a unique precursory center is hence excited.

As elaborated above, although the SCS SSTA is relatively small in magnitude, its effect on PNA is rather conspicuous, almost comparable to that of ENSO. This remarkable

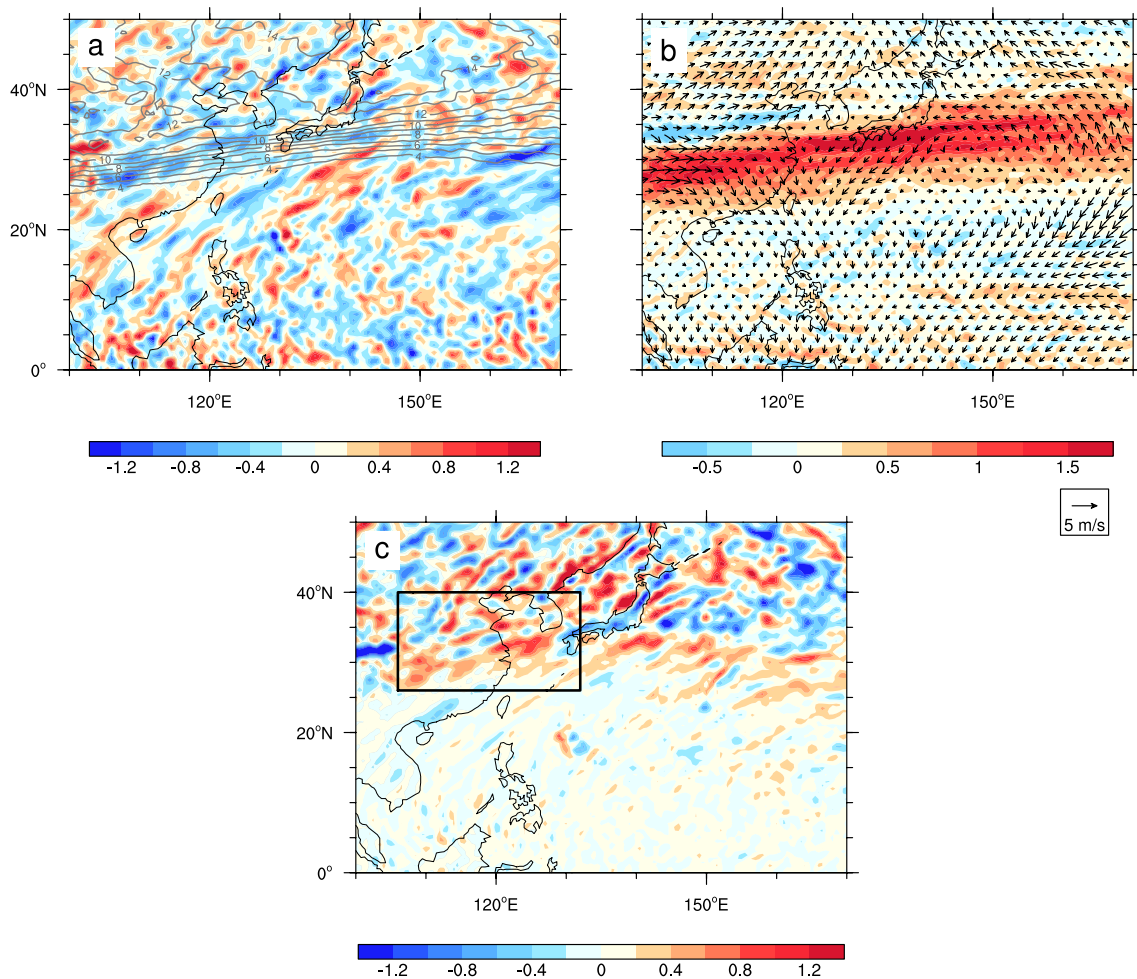


Fig. 11 As in Fig. 10, but for the negative phase on day -20

finding is consistent with previous reports. For example, as suggested, even small changes in SST are capable of leading to large-scale convection modulation and thus large anomalies in atmospheric response (Trenberth et al. 1998). Also by Newman and Sardeshmukh (1998), the sensitive area of tropical forcing for PNA response could shift westward over time in winter, and the sensitivity to smaller-scale forcing increases.

5 Summary

The Pacific–North American (PNA) teleconnection pattern has recently been found to be remarkably influenced by the South China Sea (SCS) sea surface temperature anomaly (SSTA) (Zhang and Liang 2021). This study further demonstrates that, the SCS SSTA does not merely impact PNA but also induces a new type of PNA response, in addition to those as induced by, say, ENSO, in the PNA continuum.

Through composite analysis, we show that the SCS-induced PNA pattern and its evolution are distinctly different from the ENSO-induced and conventional counterparts. Generally, the centers of the SCS-induced PNA are more scattered in distribution. Most of all, they seem to follow well the great circle route as predicted by the classical theory by Hoskins and Karoly (1981), in contrast to the conventional PNA patterns. For the evolution, a more zonally oriented new pathway is displayed: the positive (negative)-phase SCS-induced PNA is led by a unique precursory anti-cyclonic (cyclonic) center to the northeast of SCS, which propagates downstream along the Asian westerly jet; afterwards, the wave amplification and dispersion take place at the jet exit, and with energy propagation, the PNA pattern eventually matures. The asymmetry in amplitude and lifetime for two phases of PNA also appears.

Also investigated are the processes for the SCS to trigger the PNA response through air-sea interaction. The positive (negative) SCS SSTA modulates the atmospheric diabatic heating through the anomalous surface heat flux,

and then an anomalous upper-level atmospheric divergence (convergence) is aroused, which then generates a negative (positive) wave source, and subsequently induces an anticyclonic (cyclonic) vortex. This is the precursory anticyclonic (cyclonic) center that eventually leads to the formation of a new positive (negative) PNA response.

It merits mentioning that, although the SCS SSTA is relatively small in magnitude, its effect on PNA is rather conspicuous, almost comparable to that of ENSO.

All in all, we have shown that the SCS SSTA will excite a new type of PNA pattern, which seems to be more consistent with the classical theory by Hoskins and Karoly (1981). We have also shown that how this excitation works. It should be pointed out that, after the initiation, many other mechanisms may come in play. For instance, the barotropic amplification especially at the jet exit can contribute to its rapid growth (e.g., Simmons et al. 1983; Branstator 1992); the role of transient eddy feedback is also important in maintaining the pattern (e.g., Dai et al. 2017; Guo et al. 2020); moreover, strong transient eddy activities can accelerate the westerly jet (e.g., Ren et al. 2008; Chen et al. 2019; Wang et al. 2019) and hence may also exert influence on the SCS-induced PNA. These issues, among others, which involve nonlinear interactions between a multitude of scales, will be investigated in the near future using a recently developed multiscale window transform (MWT) and the rigorously MWT-based localized energetics analysis (Liang and Anderson 2007; Liang 2016).

Acknowledgements We appreciate the suggestions by an anonymous reviewer. Yinchun Zhang thanks Yineng Rong, Yuhui Zhao, and Weibang He for helpful suggestions. The reanalysis data are made available by ECMWF, and the computing resources are provided by the Supercomputing Center of Nanjing University of Information Science and Technology, to whom we are grateful. This work was supported by the National Natural Science Foundation of China (Grant Nos. 41975064, 42230105), the Shanghai International Science and Technology Partnership Project (Grant No. 21230780200), and the startup funds to XSL by Fudan University and Southern Marine Science and Engineering Guangdong Laboratory (Zhuhai).

Funding National Natural Science Foundation of China, 41975064, X. San Liang, 42230105, X. San Liang, Shanghai International Science and Technology Partnership Project, 21230780200, X. San Liang, Fudan University Startup Fund, X. San Liang, Southern Marine Science and Engineering Guangdong Laboratory (Zhuhai) Startup Fund, X. San Liang.

Data availability statement The ERA5 reanalysis dataset used for this study is available at <https://cds.climate.copernicus.eu/cdsapp#!/dataset/reanalysis-era5-pressure-levels?tab=overview>.

Declarations

Conflict of interest The authors have not disclosed any conflict of interest.

References

- Alexander MA, Bladé I, Newman M et al (2002) The Atmospheric bridge: the influence of enso teleconnections on air-sea interaction over the global oceans. *J Clim* 15:2205–2231. [https://doi.org/10.1175/1520-0442\(2002\)015%3c2205:TABTIO%3e2.0.CO;2](https://doi.org/10.1175/1520-0442(2002)015%3c2205:TABTIO%3e2.0.CO;2)
- Ashok K, Behera SK, Rao SA et al (2007) El Niño modoki and its possible teleconnection. *J Geophys Res Oceans* 112:C11007. <https://doi.org/10.1029/2006JC003798>
- Athanasiadis PJ, Wallace JM, Wettstein JJ (2010) Patterns of winter-time jet stream variability and their relation to the storm tracks. *J Atmos Sci* 67:1361–1381. <https://doi.org/10.1175/2009JAS3270.1>
- Barnston AG, Livezey RE (1987) Classification, seasonality and persistence of low-frequency atmospheric circulation patterns. *Mon Wea Rev* 115:1083–1126. [https://doi.org/10.1175/1520-0493\(1987\)115%3c1083:CSAPOL%3e2.0.CO;2](https://doi.org/10.1175/1520-0493(1987)115%3c1083:CSAPOL%3e2.0.CO;2)
- Barsugli JJ, Sardeshmukh PD (2002) Global atmospheric sensitivity to tropical sst anomalies throughout the Indo-Pacific basin. *J Clim* 15:3427–3442. [https://doi.org/10.1175/1520-0442\(2002\)015%3c3427:GASTTS%3e2.0.CO;2](https://doi.org/10.1175/1520-0442(2002)015%3c3427:GASTTS%3e2.0.CO;2)
- Baxter S, Nigam S (2013) A subseasonal teleconnection analysis: PNA development and its relationship to the NAO. *J Clim* 26:6733–6741. <https://doi.org/10.1175/JCLI-D-12-00426.1>
- Branstator G (1983) Horizontal energy propagation in a barotropic atmosphere with meridional and zonal structure. *J Atmos Sci* 40:1689–1708. [https://doi.org/10.1175/1520-0469\(1983\)040%3c1689:HEPIAB%3e2.0.CO;2](https://doi.org/10.1175/1520-0469(1983)040%3c1689:HEPIAB%3e2.0.CO;2)
- Branstator G (1992) The maintenance of low-frequency atmospheric anomalies. *J Atmos Sci* 49:1924–1946. [https://doi.org/10.1175/1520-0469\(1992\)049%3c1924:TMOLFA%3e2.0.CO;2](https://doi.org/10.1175/1520-0469(1992)049%3c1924:TMOLFA%3e2.0.CO;2)
- Branstator G (2014) Long-lived response of the midlatitude circulation and storm tracks to pulses of tropical heating. *J Clim* 27:8809–8826. <https://doi.org/10.1175/JCLI-D-14-00312.1>
- Chen Z, Gan B, Wu L, Jia F (2018) Pacific-North American teleconnection and North Pacific oscillation: historical simulation and future projection in CMIP5 models. *Clim Dyn* 50:4379–4403. <https://doi.org/10.1007/s00382-017-3881-9>
- Chen Q, Hu H, Ren X, Yang X-Q (2019) Numerical simulation of midlatitude upper-level zonal wind response to the change of North Pacific subtropical front strength. *J Geophys Res Atmos* 124:4891–4912. <https://doi.org/10.1029/2018JD029589>
- Corti S, Palmer TN (1997) Sensitivity analysis of atmospheric low-frequency variability. *Quart J Roy Meteor Soc* 123:2425–2447. <https://doi.org/10.1002/qj.49712354413>
- Cronin MF, Gentemann CL, Edson J et al (2019) Air-sea fluxes with a focus on heat and momentum. *Front Mar Sci* 6:430. <https://doi.org/10.3389/fmars.2019.00430>
- Dai Y, Feldstein SB, Tan B, Lee S (2017) Formation mechanisms of the Pacific-North American teleconnection with and without its canonical tropical convection pattern. *J Clim* 30:3139–3155. <https://doi.org/10.1175/JCLI-D-16-0411.1>
- Drouard M, Rivière G, Arbogast P (2015) The link between the North Pacific climate variability and the North Atlantic oscillation via downstream propagation of synoptic waves. *J Clim* 28:3957–3976. <https://doi.org/10.1175/JCLI-D-14-00552.1>
- Feldstein SB (2000) The timescale, power spectra, and climate noise properties of teleconnection patterns. *J Clim* 13:4430–4440. [https://doi.org/10.1175/1520-0442\(2000\)013%3c4430:TTPSAC%3e2.0.CO;2](https://doi.org/10.1175/1520-0442(2000)013%3c4430:TTPSAC%3e2.0.CO;2)
- Feldstein SB (2002) Fundamental mechanisms of the growth and decay of the PNA teleconnection pattern. *Quart J Roy Meteor Soc* 128:775–796. <https://doi.org/10.1256/0035900021643683>
- Gong S, Hagan DFT, Zhang C (2019) Analysis on precipitable water vapor over the tibetan plateau using FengYun-3A medium

- resolution spectral imager products. *J Sens* 2019:e6078591. <https://doi.org/10.1155/2019/6078591>
- Guo Y, Wen Z, Tan Y, Li X (2020) Plausible causes of the interdecadal change of the North Pacific teleconnection pattern in boreal spring around the late 1990s. *Clim Dyn* 55:1427–1442. <https://doi.org/10.1007/s00382-020-05334-y>
- He Z, Wu R (2013) Seasonality of interannual atmosphere–ocean interaction in the South China Sea. *J Oceanogr* 69:699–712. <https://doi.org/10.1007/s10872-013-0201-9>
- Hersbach H, Bell B, Berrisford P et al (2020) The ERA5 global reanalysis. *Quart J Roy Meteor Soc* 146:1999–2049. <https://doi.org/10.1002/qj.3803>
- Horel JD, Wallace JM (1981) Planetary-scale atmospheric phenomena associated with the Southern oscillation. *Mon Wea Rev* 109:813–829. [https://doi.org/10.1175/1520-0493\(1981\)109%3c0813:PSA-PAW%3e2.0.CO;2](https://doi.org/10.1175/1520-0493(1981)109%3c0813:PSA-PAW%3e2.0.CO;2)
- Hoskins BJ, Ambrizzi T (1993) Rossby wave propagation on a realistic longitudinally varying flow. *J Atmos Sci* 50:1661–1671. [https://doi.org/10.1175/1520-0469\(1993\)050%3c1661:RWPOAR%3e2.0.CO;2](https://doi.org/10.1175/1520-0469(1993)050%3c1661:RWPOAR%3e2.0.CO;2)
- Hoskins BJ, Karoly DJ (1981) The steady linear response of a spherical atmosphere to thermal and orographic forcing. *J Atmos Sci* 38:1179–1196. [https://doi.org/10.1175/1520-0469\(1981\)038%3c1179:TSLROA%3e2.0.CO;2](https://doi.org/10.1175/1520-0469(1981)038%3c1179:TSLROA%3e2.0.CO;2)
- Johnson NC, Feldstein SB (2010) The continuum of North Pacific sea level pressure patterns: intraseasonal, interannual, and interdecadal variability. *J Clim* 23:851–867. <https://doi.org/10.1175/2009JCLI3099.1>
- L'Heureux ML, Kumar A, Bell GD et al (2008) Role of the Pacific–North American (PNA) pattern in the 2007 Arctic sea ice decline. *Geophys Res Lett* 35:L20701. <https://doi.org/10.1029/2008GL035205>
- Leathers DJ, Yarnal B, Palecki MA (1991) The Pacific/North American teleconnection pattern and United States climate. part i: regional temperature and precipitation associations. *J Clim* 4:517–528. [https://doi.org/10.1175/1520-0442\(1991\)004%3c0517:TPATPA%3e2.0.CO;2](https://doi.org/10.1175/1520-0442(1991)004%3c0517:TPATPA%3e2.0.CO;2)
- Li X, Hu Z-Z, Liang P, Zhu J (2019) Contrastive influence of ENSO and PNA on variability and predictability of North American winter precipitation. *J Clim* 32:6271–6284. <https://doi.org/10.1175/JCLI-D-19-0033.1>
- Lian T, Chen D (2012) An evaluation of rotated EOF analysis and its application to tropical Pacific SST variability. *J Clim* 25:5361–5373. <https://doi.org/10.1175/JCLI-D-11-00663.1>
- Liang XS (2016) Canonical transfer and multiscale energetics for primitive and quasigeostrophic atmospheres. *J Atmos Sci* 73:4439–4468. <https://doi.org/10.1175/JAS-D-16-0131.1>
- Liang XS, Anderson DGM (2007) Multiscale window transform. *Multiscale Model Simul* 6:437–467. <https://doi.org/10.1137/06066895X>
- Liu Q, Jiang X, Xie S-P, Liu WT (2004) A gap in the Indo-Pacific warm pool over the South China Sea in boreal winter: seasonal development and interannual variability. *J Geophys Res Oceans* 109:C07012. <https://doi.org/10.1029/2003JC002179>
- Liu Z, Tang Y, Jian Z et al (2017) Pacific North American circulation pattern links external forcing and North American hydroclimatic change over the past millennium. *Proc Natl Acad Sci USA* 114:3340–3345. <https://doi.org/10.1073/pnas.1618201114>
- Luo D, Ge Y, Zhang W, Dai A (2020) A unified nonlinear multiscale interaction model of Pacific–North American teleconnection patterns. *J Atmos Sci* 77:1387–1414. <https://doi.org/10.1175/JAS-D-19-0312.1>
- Mori M, Watanabe M (2008) The growth and triggering mechanisms of the PNA: a MJO–PNA coherence. *J Meteor Soc Jpn* 86:213–236. <https://doi.org/10.2151/jmsj.86.213>
- Newman M, Sardeshmukh PD (1998) The impact of the annual cycle on the North Pacific/North American response to remote low-frequency forcing. *J Atmos Sci* 55:1336–1353. [https://doi.org/10.1175/1520-0469\(1998\)055%3c1336:TOTAC%3e2.0.CO;2](https://doi.org/10.1175/1520-0469(1998)055%3c1336:TOTAC%3e2.0.CO;2)
- Palmer TN (1988) Medium and extended range predictability and stability of the Pacific/North American mode. *Quart J Roy Meteor Soc* 114:691–713. <https://doi.org/10.1002/qj.49711448108>
- Ren X, Zhang Y, Xiang Y (2008) Connections between wintertime jet stream variability, oceanic surface heating, and transient eddy activity in the North Pacific. *J Geophys Res Atmos* 113:D21119. <https://doi.org/10.1029/2007JD009464>
- Renshaw AC, Rowell DP, Folland CK (1998) Wintertime low-frequency weather variability in the North Pacific–American sector 1949–93. *J Clim* 11:1073–1093. [https://doi.org/10.1175/1520-0442\(1998\)011%3c1073:WLFWVI%3e2.0.CO;2](https://doi.org/10.1175/1520-0442(1998)011%3c1073:WLFWVI%3e2.0.CO;2)
- Roxy M, Tanimoto Y (2012) Influence of sea surface temperature on the intraseasonal variability of the South China Sea summer monsoon. *Clim Dyn* 39:1209–1218. <https://doi.org/10.1007/s00382-011-1118-x>
- Sardeshmukh PD, Hoskins BJ (1988) The generation of global rotational flow by steady idealized tropical divergence. *J Atmos Sci* 45:1228–1251. [https://doi.org/10.1175/1520-0469\(1988\)045%3c1228:TGGRF%3e2.0.CO;2](https://doi.org/10.1175/1520-0469(1988)045%3c1228:TGGRF%3e2.0.CO;2)
- Shukla J, Wallace JM (1983) Numerical simulation of the atmospheric response to equatorial Pacific sea surface temperature anomalies. *J Atmos Sci* 40:1613–1630. [https://doi.org/10.1175/1520-0469\(1983\)040%3c1613:NSOTAR%3e2.0.CO;2](https://doi.org/10.1175/1520-0469(1983)040%3c1613:NSOTAR%3e2.0.CO;2)
- Simmons AJ, Wallace JM, Branstator GW (1983) Barotropic wave propagation and instability, and atmospheric teleconnection patterns. *J Atmos Sci* 40:1363–1392. [https://doi.org/10.1175/1520-0469\(1983\)040%3c1363:BWPAIA%3e2.0.CO;2](https://doi.org/10.1175/1520-0469(1983)040%3c1363:BWPAIA%3e2.0.CO;2)
- Straus DM, Shukla J (2002) Does ENSO force the PNA? *J Clim* 15:2340–2358. [https://doi.org/10.1175/1520-0442\(2002\)015%3c2340:DEFTP%3e2.0.CO;2](https://doi.org/10.1175/1520-0442(2002)015%3c2340:DEFTP%3e2.0.CO;2)
- Takaya K, Nakamura H (2001) A formulation of a phase-independent wave-activity flux for stationary and migratory quasigeostrophic eddies on a zonally varying basic flow. *J Atmos Sci* 58:608–627. [https://doi.org/10.1175/1520-0469\(2001\)058%3c0608:AFOAPI%3e2.0.CO;2](https://doi.org/10.1175/1520-0469(2001)058%3c0608:AFOAPI%3e2.0.CO;2)
- Trenberth KE, Branstator GW, Karoly D et al (1998) Progress during TOGA in understanding and modeling global teleconnections associated with tropical sea surface temperatures. *J Geophys Res Oceans* 103:14291–14324. <https://doi.org/10.1029/97JC01444>
- Wallace JM, Gutzler DS (1981) Teleconnections in the geopotential height field during the Northern hemisphere winter. *Mon Wea Rev* 109:784–812. [https://doi.org/10.1175/1520-0493\(1981\)109%3c0784:TITGHF%3e2.0.CO;2](https://doi.org/10.1175/1520-0493(1981)109%3c0784:TITGHF%3e2.0.CO;2)
- Wang G, Su J, Ding Y, Chen D (2007) Tropical cyclone genesis over the south China Sea. *J Mar Syst* 68:318–326. <https://doi.org/10.1016/j.jmarsys.2006.12.002>
- Wang L, Hu H, Yang X (2019) The atmospheric responses to the intensity variability of subtropical front in the wintertime North Pacific. *Clim Dyn* 52:5623–5639. <https://doi.org/10.1007/s00382-018-4468-9>
- Weng H, Behera SK, Yamagata T (2009) Anomalous winter climate conditions in the Pacific rim during recent El Niño Modoki and El Niño events. *Clim Dyn* 32:663–674. <https://doi.org/10.1007/s00382-008-0394-6>
- Wirth V, Riemer M, Chang EKM, Martius O (2018) Rossby wave packets on the midlatitude waveguide—a review. *Mon Wea Rev* 146:1965–2001. <https://doi.org/10.1175/MWR-D-16-0483.1>
- Yang G-Y, Hoskins BJ (1996) Propagation of rossby waves of nonzero frequency. *J Atmos Sci* 53:2365–2378. [https://doi.org/10.1175/1520-0469\(1996\)053%3c2365:PORWON%3e2.0.CO;2](https://doi.org/10.1175/1520-0469(1996)053%3c2365:PORWON%3e2.0.CO;2)

- Yu J-Y, Kao H-Y (2007) Decadal changes of ENSO persistence barrier in SST and ocean heat content indices: 1958–2001. *J Geophys Res Atmos* 112:D13106. <https://doi.org/10.1029/2006JD007654>
- Yu J-Y, Zou Y, Kim ST, Lee T (2012) The changing impact of El Niño on US winter temperatures. *Geophys Res Lett* 39:L15702. <https://doi.org/10.1029/2012GL052483>
- Yuan J, Tan B, Feldstein SB, Lee S (2015) Wintertime North Pacific teleconnection patterns: seasonal and interannual variability. *J Clim* 28:8247–8263. <https://doi.org/10.1175/JCLI-D-14-00749.1>
- Zhang Y, Liang XS (2021) The causal role of South China Sea on the Pacific-North American teleconnection pattern. *Clim Dyn*. <https://doi.org/10.1007/s00382-021-06070-7>

Publisher's Note Springer Nature remains neutral with regard to jurisdictional claims in published maps and institutional affiliations.

Springer Nature or its licensor (e.g. a society or other partner) holds exclusive rights to this article under a publishing agreement with the author(s) or other rightsholder(s); author self-archiving of the accepted manuscript version of this article is solely governed by the terms of such publishing agreement and applicable law.